

Eccentric Regularization: Minimizing Hyperspherical Energy without explicit projection

Xuefeng Li and Alan Blair

School of Computer Science and Engineering
University of New South Wales, Sydney, Australia
{xuefeng.li1,a.blair}@unsw.edu.au

April 26, 2021

Abstract

Several regularization methods have recently been introduced which force the latent activations of an autoencoder or deep neural network to conform to either a Gaussian or hyperspherical distribution, or to minimize the implicit rank of the distribution in latent space. In the present work, we introduce a novel regularizing loss function which simulates a pairwise repulsive force between items and an attractive force of each item toward the origin. We show that minimizing this loss function in isolation achieves a hyperspherical distribution. Moreover, when used as a regularizing term, the scaling factor can be adjusted to allow greater flexibility and tolerance of eccentricity, thus allowing the latent variables to be stratified according to their relative importance, while still promoting diversity. We apply this method of Eccentric Regularization to an autoencoder, and demonstrate its effectiveness in image generation, representation learning and downstream classification tasks.

1 Introduction

In recent years a number of regularization methods have been introduced which force the latent activations of an autoencoder or deep neural network to conform to either a hyperspherical or Gaussian distribution, in order to encourage diversity in the latent vectors, or to minimize the implicit rank of the distribution in latent space.

Variational Autoencoders (VAE) (Kingma and Welling, 2014) and related variational methods such as β -VAE (Higgins et al., 2017) force the latent distribution to match a known prior distribution by minimizing the Kullback-Leibler divergence. Normally, a standard Gaussian distribution is used as the prior, but alternatives such as the hyperspherical distribution have also been investigated in the literature due to certain advantages (Davidson et al., 2018). More recently, deterministic alternatives have been proposed such as Wasserstein AutoEncoder (WAE) (Tolstikhin et al., 2018), VQ-VAE (van den Oord et al., 2017) and RAE (Ghosh et al., 2020).

Several existing methods encourage diversity by maximizing pairwise dissimilarity between items, drawing inspiration in part from a 1904 paper by J.J. Thomson in which various classical models are proposed for maintaining the electrons of an atom in an appropriate formation around the nucleus (Thomson, 1904). Hyperspherical Energy Minimization (Liu et al., 2018) has been used to regularize the hidden unit

activations in deep networks, with a Thomson-like loss function which projects each vector onto a hypersphere and simulates a repulsive force pushing these projected items away from each other and spreading them evenly around the sphere. Other methods use an implicit projection by optimizing for the cosine similarity between vectors (Yu et al., 2011; Bao et al., 2013; Xie et al., 2015).

Recently, new compressive techniques have been developed with the aim of minimizing the intrinsic dimension of the latent space. This can be achieved by introducing projection mappings (Lin et al., 2020) or additional linear layers between the encoder and decoder (Jing et al., 2020), or by other methods such as optimizing for a variational lower bound on the mutual information between datapoints (Grover and Ermon, 2019).

The word *eccentricity* (sometimes also called “unevenness” (Xie et al., 2017)) can be used as a general term for the extent to which the spectrum of the covariance matrix in latent space differs from that of a hyperspherical or standard normal distribution. Methods such as VAE aim to give equal importance to all latent features, while compressive techniques like IRMAE (Jing et al., 2020) explicitly encourage some features to become dominant while others diminish.

In the present work, we introduce a novel regularizing loss function which has the following properties:

- (a) When its weighting factor is large, it assigns equal importance to all latent features, by forcing them to conform to a hyperspherical distribution.
- (b) When its weighting factor is reduced, it becomes tolerant to variation in the relative importance of different latent features, while continuing to promote diversity.

Using our method as a regularizer for deep autoencoders, we explore how this tolerance to eccentricity enables the latent features (eigenvectors) to be stratified according to their relative importance (eigenvalue) so that the same, or very similar, features are extracted when the algorithm is re-run with different initial weights. We demonstrate the effectiveness of our method for image generation and downstream classification tasks, and discuss its potential use for data visualization and analysis.

2 Eccentric Loss Function

We consider a family of loss functions $l_{\mu,N}$ on a set of b items $\mathbf{z}_i \in \mathbb{R}^d$ of the form:

$$l_{\mu,N}(\{\mathbf{z}_i\}) = \frac{1}{b(b-1)} \sum_{\mathbf{z}_i \neq \mathbf{z}_j} K_{\mu,N}(\mathbf{z}_i, \mathbf{z}_j)$$

where

$$K_{\mu,N}(\mathbf{z}_i, \mathbf{z}_j) = \left(\frac{\|\mathbf{z}_i\|^2 + \|\mathbf{z}_j\|^2}{2} \right) - \mu N \log \left(1 + \frac{\|\mathbf{z}_i - \mathbf{z}_j\|^2}{N} \right). \quad (1)$$

Note that the gradient of $K_{\mu,N}$ effectively simulates a repulsive force between all pairs of items $\mathbf{z}_i, \mathbf{z}_j$, equal to $2\mu(\mathbf{z}_i - \mathbf{z}_j)/(1 + \|\mathbf{z}_i - \mathbf{z}_j\|^2/N)$, and an attractive force $(-\mathbf{z}_i)$ of each item \mathbf{z}_i toward the origin.

Equation (1) ostensibly has two free parameters μ and N , but we intend to set N as a function of μ and the dimension d in such a way that the loss function is minimized on a hyperspherical distribution of radius approximately \sqrt{d} , which is a close approximation (in the sense of Wasserstein distance) to the Standard Normal distribution. The relationship between μ , N and the radius ρ of the stationary spherical distribution is determined by this theorem:

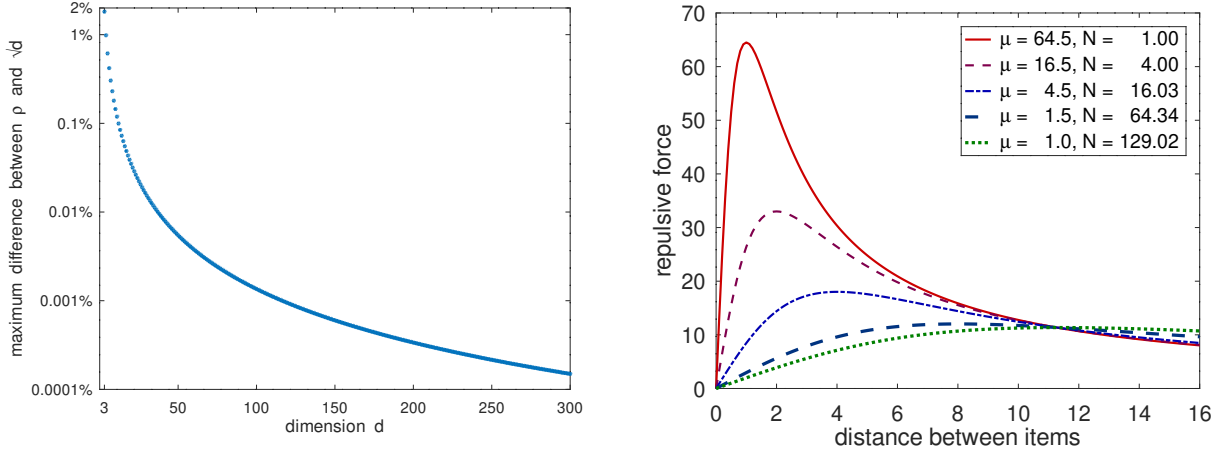


Figure 1: Maximum (percent) difference between ρ and \sqrt{d} . Figure 2: Repulsive force between pairs of items ($d = 64$).

Theorem 1. Let S_ρ denote the uniform distribution on a hypersphere of radius ρ in dimension $d \geq 3$, and let $\Gamma(\cdot)$ denote the Gamma Function. Then S_ρ is a stationary point for $l_{\mu,N}$, provided ρ satisfies the following equation:

$$\frac{N}{\rho^2 \sqrt{\pi}} \frac{\Gamma(\frac{d}{2})}{\Gamma(\frac{d-1}{2})} \int_{u=1}^{1+\frac{4\rho^2}{N}} \frac{(\frac{N}{2\rho^2}(u-1))^{\frac{d-1}{2}} (2 - \frac{N}{2\rho^2}(u-1))^{\frac{d-3}{2}}}{u} du = \frac{1}{\mu}.$$

Proof: (see Appendix)

Our aim is to choose N in such a way that the radius ρ of the stable spherical distribution for $l_{\mu,N}$ is very close to \sqrt{d} . Our choice for N is:

$$N = 2d(1 + \frac{1}{2\mu(d-1)})/(2\mu - 1).$$

(The motivation for this choice is explained in the Appendix).

In order to test the accuracy of this approximation, we set N as above and compute ρ using numerical integration and bisection, for each dimension d and for all values of μ between 1 and $2d + 1$ (in increments of 0.01). Figure 1 shows the percentage difference between ρ and \sqrt{d} , maximized over μ , for d between 3 and 300. We see that ρ is within 0.1% of \sqrt{d} for $d \geq 12$, within 0.01% for $d \geq 38$, and within 0.001% for $d \geq 117$.

3 Regularization, Local Flexibility and Tolerance to Eccentricity

We are primarily interested in the eccentric loss function for the purpose of regularization, as part of an overall loss function of the form

$$\text{loss} = \text{loss}_{\text{other}} + \lambda l_{\mu,N}(\{\mathbf{z}_i\}).$$

The scaling factor λ and the combination μ, N regulate both the local flexibility of the distribution and its tolerance to eccentricity. Figure 2 shows the magnitude of the repulsive force between any two items based

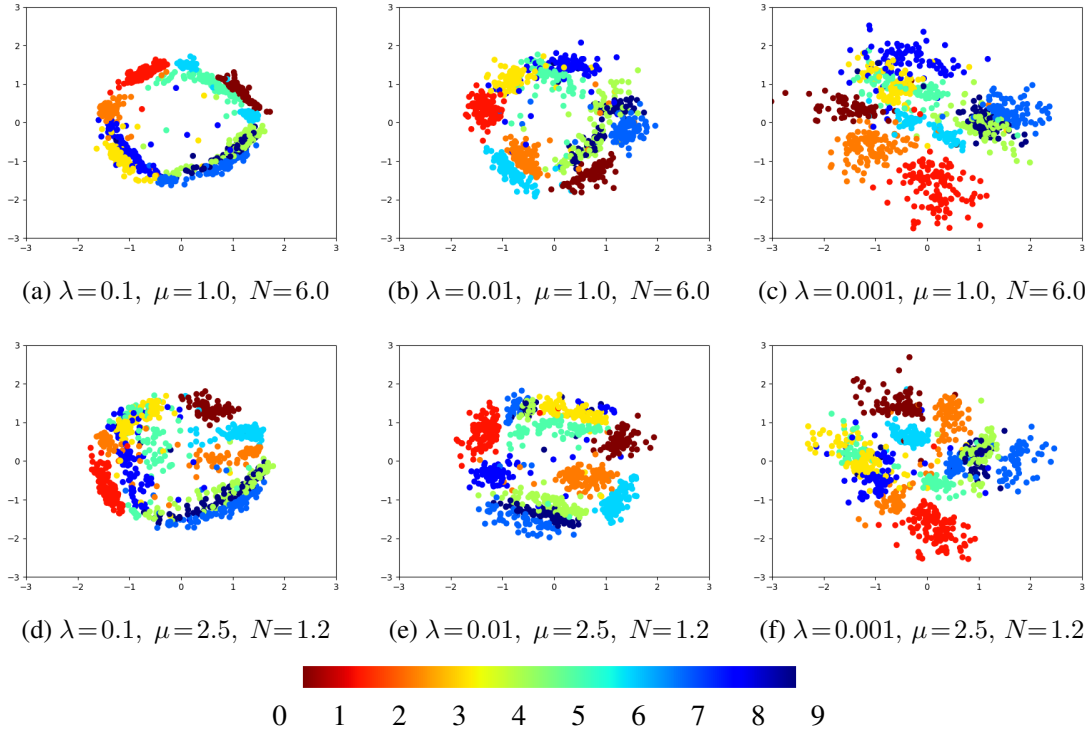


Figure 3: Distribution in latent space of a random selection of test items, for Eccentric Autoencoder trained on the MNIST dataset using two latent dimensions, with $\lambda = 0.1, 0.01$ or 0.001 and $\mu = 1.0$ or 2.5 . The horizontal and vertical axes are the principal components corresponding to the larger and smaller eigenvalue of the covariance matrix.

on the distance between them. Note that the repulsive force increases until a distance of \sqrt{N} and decreases thereafter. At one extreme, where $\mu = d + \frac{1}{2}$ and $N \simeq 1$, the repulsive force is strongest for nearby items, thus forcing them to spread out evenly on both a local and global scale. At the other extreme, where $\mu = 1$ and $N \simeq 2d + 1$, each item is influenced most strongly by items that are far away. This “action at a distance” forces the items to spread out on a global scale but allows some flexibility on a local scale. Figure 3 illustrates the behavior of this regularization in the case where $\text{loss}_{\text{other}}$ is the L_2 distance between the original and reconstructed images for an autoencoder trained on the MNIST dataset, with $d = 2$ (see section 4 for further details). When λ is large (left column) the distribution conforms closely to a sphere of radius \sqrt{d} . As λ decreases (middle column) the distribution deviates from the sphere but starts to roughly approximate a standard normal distribution. When λ decreases further (right column) the distribution becomes more flexible, forcing the items to spread out on a global scale but allowing clusters and gaps to form at a local scale. The eccentricity also increases, allowing greater variance in some directions than others, especially when $\mu = 1$ (Figure 3(c)).

We find experimentally that this tolerance of our loss function to increased eccentricity occurs for any dimension d , provided the trace of the covariance matrix is approximately equal to d . This can be explained intuitively as follows: Consider a point $\mathbf{z} = (\sqrt{d}, 0, \dots, 0)$ on the sphere $\mathcal{S}_{\sqrt{d}}$ of radius \sqrt{d} (see Figure 4). Since the density of $\mathcal{S}_{\sqrt{d}}$ is heavily concentrated in vectors nearly perpendicular to \mathbf{z} , we can think of a “typical” point $\mathbf{z}_{\perp} \in \mathcal{S}_{\sqrt{d}}$ as being nearly perpendicular to \mathbf{z} and exerting a repulsive force on \mathbf{z} whose

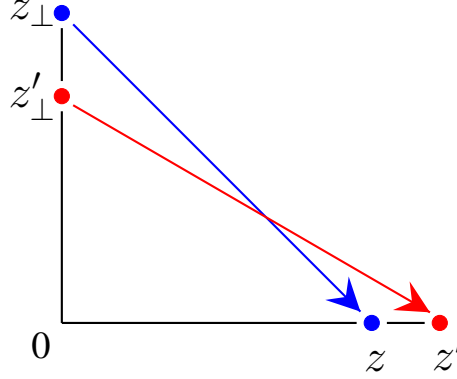


Figure 4: The point $\mathbf{z} = (\sqrt{d}, 0, \dots, 0)$ is repelled by a “typical” point \mathbf{z}_\perp on the sphere $\mathcal{S}_{\sqrt{d}}$ with a force whose radial component approximately balances the attractive force $(-\mathbf{z})$; when the sphere $\mathcal{S}_{\sqrt{d}}$ is transformed to an ellipse with covariance $\Sigma = \text{diag}(\sigma_1^2, \dots, \sigma_d^2)$ with $\text{Trace}(\Sigma) = \sum_i \sigma_i^2 = d$, the transformed points $\mathbf{z}', \mathbf{z}'_\perp$ satisfy $\|\mathbf{z}' - \mathbf{z}'_\perp\| \simeq \|\mathbf{z} - \mathbf{z}_\perp\|$ and the radial component continues to approximate the (new) attractive force $(-\mathbf{z}')$.

component in the direction of \mathbf{z} is approximately

$$2\mu \mathbf{z} / (1 + \|\mathbf{z} - \mathbf{z}_\perp\|^2/N) \simeq \mathbf{z} (2\mu / (1 + 2d/N)) \simeq \mathbf{z}.$$

When these forces are aggregated, the transverse components cancel each other out while the radial components combine to exactly balance the attractive force of $(-\mathbf{z})$. The influence of these “typical” points is particularly dominant when $\mu = 1$, because in this case the pairwise repulsive force also reaches its maximum at a distance of approximately $\sqrt{2d}$ (see Figure 2).

Now suppose that the sphere $\mathcal{S}_{\sqrt{d}}$ is transformed into an ellipse with covariance $\Sigma^{\frac{1}{2}}$, where $\text{Trace}(\Sigma) = d$, and assume for simplicity that $\Sigma = \text{diag}(\sigma_1^2, \dots, \sigma_d^2)$ is diagonal. The transformation $\Sigma^{\frac{1}{2}}$ maps \mathbf{z} to $\mathbf{z}' = (\sigma_1 \sqrt{d}, 0, \dots, 0)$, and the condition $\sum_i \sigma_i^2 = \text{Trace}(\Sigma) = d$ ensures that the “typical” point \mathbf{z}_\perp will be mapped to a point \mathbf{z}'_\perp for which $\|\mathbf{z}' - \mathbf{z}'_\perp\| \simeq \|\mathbf{z} - \mathbf{z}_\perp\|$. But, due to the change in angle, the radial component of the repulsive force will change from $(-\mathbf{z})$ to $(-\mathbf{z}')$, keeping it in balance with the attractive force.

4 Autoencoder Experiments

In this section, we explore the eccentric loss function as a method for regularizing the latent variables of an autoencoder. The loss function in this case is:

$$\text{loss} = \text{loss}_{\text{recon}} + \lambda l_{\mu, N}(\{\mathbf{z}_i\}),$$

where $\text{loss}_{\text{recon}}$ is the L_2 distance between the original and reconstructed image, for a training batch $\{\mathbf{z}_i\}$. Specifically, we train Eccentric Autoencoders on:

- (a) MNIST dataset (LeCun et al., 1998) for 1000 epochs using $\lambda = 0.001, \mu = 1.0$, with dimension $d = 2, 4, 6, 8$;
- (b) CelebA dataset (Liu et al., 2015) for 100 epochs using $\lambda = 0.0001, 0.001, \mu = 1.0, 1.5, 4.5, 16.5, 64.5$, with dimension $d = 64$.

λ	μ	N	runs	standard	matched
0.0001	1.0	129.02	4	55.5 ± 1.0	49.3 ± 0.8
	1.5	64.34	2	54.0 ± 0.1	48.7 ± 0.1
	4.5	16.03	2	54.3 ± 0.6	49.4 ± 0.6
	16.5	4.00	2	53.8 ± 0.1	49.4 ± 0.2
	64.5	1.00	4	54.5 ± 0.6	49.8 ± 0.4
Aggregate:			14	54.6 ± 0.9	49.4 ± 0.6
0.001	1.0	129.02	4	53.7 ± 0.3	50.2 ± 0.5
	1.5	64.34	2	52.8 ± 0.3	50.2 ± 0.5
	4.5	16.03	2	52.8 ± 0.6	51.0 ± 0.5
	16.5	4.00	2	51.5 ± 0.4	50.2 ± 0.1
	64.5	1.00	4	51.8 ± 0.4	50.3 ± 0.5
Aggregate:			14	52.6 ± 0.9	50.3 ± 0.5

Table 1: Fréchet Inception Score for CelebA.

Details of network architectures and metaparameters are given in the Appendix. Each MNIST run takes approximately 3 hours on a GeForce GTX 1080 Ti; each CelebA run takes approximately 6 hours on one node of a V100 GPU.

4.1 Image Generation

We use two different sampling methods to generate our synthetic images: *standard* sampling, where the random vectors are drawn from a standard normal distribution, and *matched* sampling, where the vectors are instead drawn from a multivariate Gaussian whose mean and covariance match those of the encoded latent vectors for the real images. Table 1 shows the Fréchet Inception Scores (Heusel et al., 2017) for $\lambda = 0.0001$ and $\lambda = 0.001$, with μ ranging between 1.0 and 64.5. We see that:

- (a) The Fréchet Inception Score for matched sampling is lower (better) than for standard sampling.
- (b) The standard sampling score is better with $\lambda = 0.001$ but the matched sampling score is better with $\lambda = 0.0001$.
- (c) There is no significant change in score for different values of μ .

4.2 Spectrum and Principal Components

Figure 5 shows the eigenvalues for the covariance matrix of the CelebA images in latent space, for different values of λ and μ . We see that the eigenvalues become more uniform (closer to 1.0) as λ increases and, to a lesser extent, as μ increases. When λ and μ decrease, the distribution becomes more eccentric, with eigenvalues ranging as high as 3.24 and as low as 0.47. As discussed in Section 3, the sum of the eigenvalues (indicated by the area under the curve) is approximately equal to the dimension d . Note that in each case the

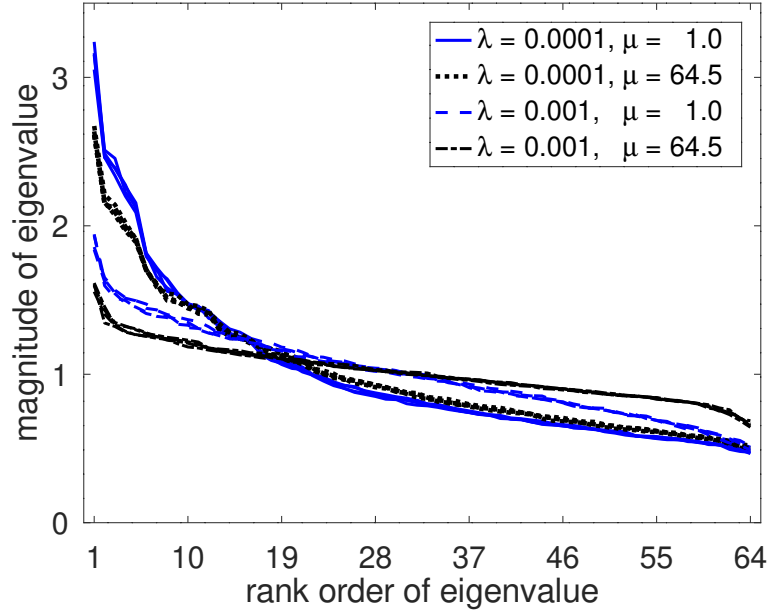


Figure 5: Spectrum of latent variable covariance matrix for Eccentric Autoencoders trained on CelebA; four independent runs are superimposed for each combination of λ and μ .

curves from four independent runs match each other almost exactly, indicating that the spectrum is largely invariant from one run to another.

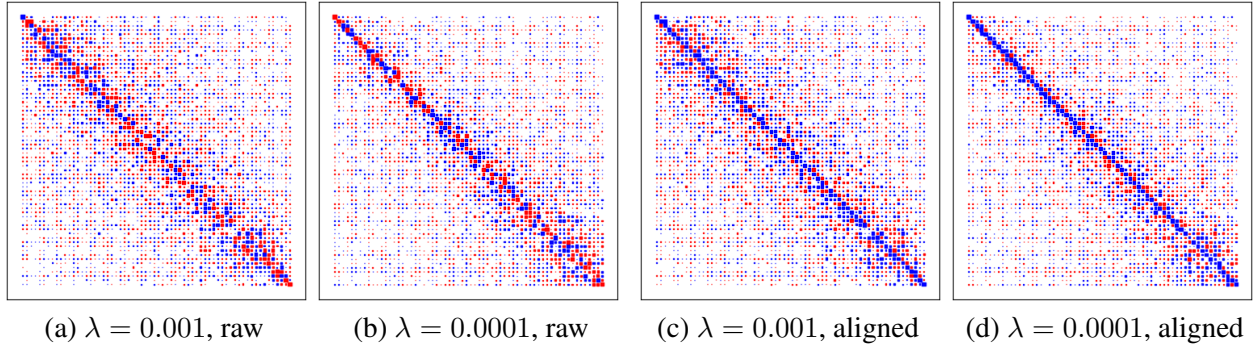


Figure 6: Cross correlation between deep principal components for Eccentric Autoencoders with $\mu = 1$ and $\lambda = 0.001$ or 0.0001 , trained independently on the CelebA dataset from different random initial weights, before the alignment procedure and afterwards.

If we shift and rotate the latent vectors of the training items so that their mean becomes zero and their coordinate axes lie along the eigenvectors of the covariance matrix in decreasing order, we can extract pairs of deep eigen-digits or eigen-faces by choosing appropriately scaled positive and negative basis vectors along each of these principal axes.






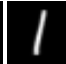



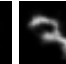





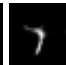




(a) $d = 6$						(b) $d = 4$			
									
p_1	p_2	p_3	p_4	p_5	p_6	p_1	p_2	p_3	p_4
(1.21)	(1.09)	(1.02)	(0.99)	(0.90)	(0.52)	(1.18)	(1.04)	(0.96)	(0.81)
(c) $d = 8$								(d) $d = 2$	
									
p_1	p_2	p_3	p_4	p_5	p_6	p_7	p_8	p_1	p_2
(1.24)	(1.19)	(1.12)	(0.98)	(0.95)	(0.92)	(0.79)	(0.65)	(1.11)	(0.90)

Figure 7: Paired eigen-digits (with corresponding eigenvalues) for deep principal components of Eccentric Autoencoders trained on MNIST with latent dimension 6, 4, 8 and 2.

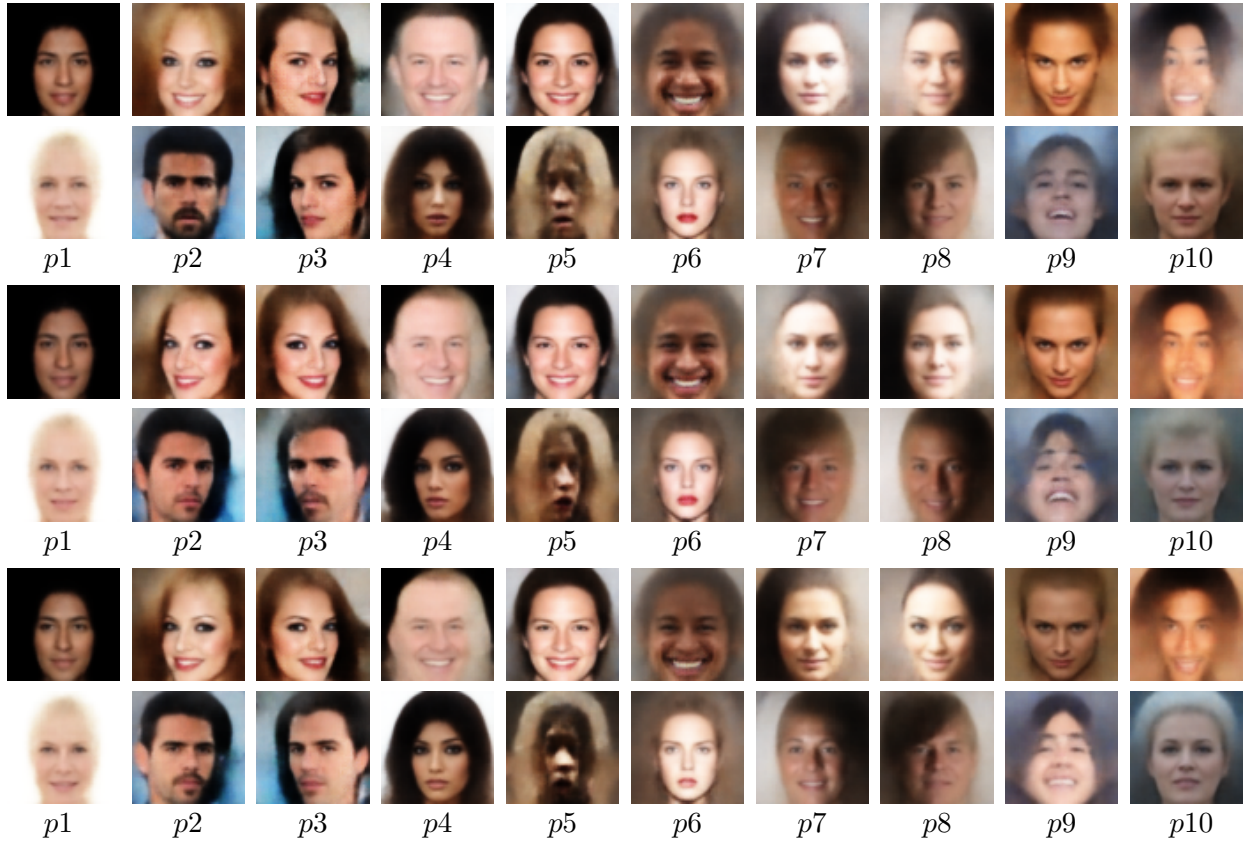


Figure 8: Paired eigen-faces corresponding to the first ten deep principal components for three Eccentric Autoencoders trained independently on CelebA from different random initial weights. We see remarkable similarity across the three runs, although there is some intermixing between neighboring components with close eigenvalues.

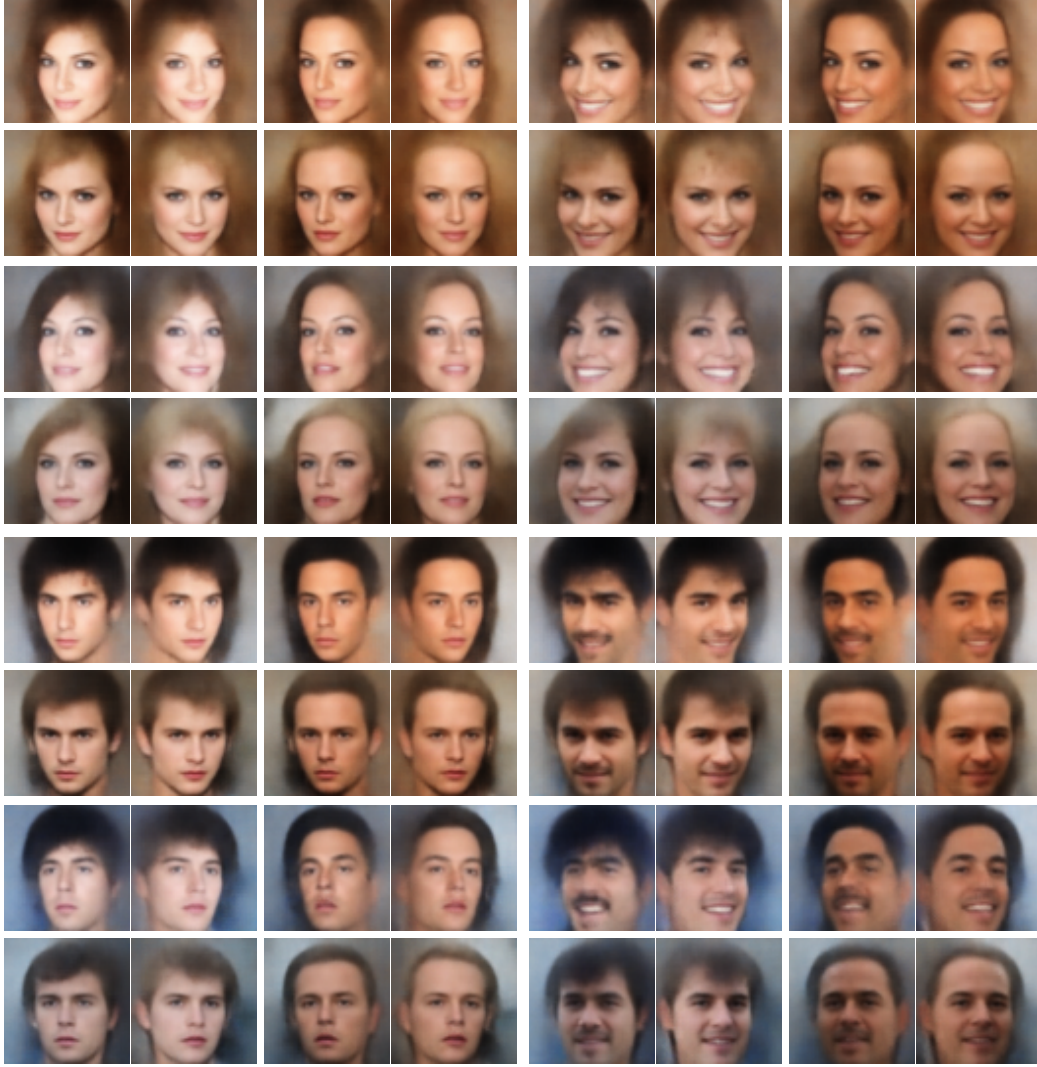


Figure 9: Images generated from principal components p_6, p_{11}, p_3 (horizontally) and p_2, p_{10}, p_9 (vertically).

We see that the eigen-digits for MNIST often look similar across different runs, even with different latent dimensions (Figure 7). The eigen-faces for CelebA also look very similar from one run to another (Figure 8).

The full mapping to the rotated latent space can be considered as an encoding which maps each input image to a vector (p_1, \dots, p_d) where p_k is the value of the coordinate in the direction of the k th (deep) principal component. We are interested in the question: How canonical is this encoding? In other words, if we train two autoencoders independently from different random weights, producing two encodings $E_1 : \text{Image} \mapsto (p_1, \dots, p_d)$ and $E_2 : \text{Image} \mapsto (q_1, \dots, q_d)$, how similar are these two mappings?

Figure 6 (a) and (b) illustrate the correlation between the principal components of two such mappings. We note that it is possible for principal components corresponding to close eigenvalues to be permuted, for example p_2 and p_3 in Figure 7 (a) and (c), which would appear as slightly off-diagonal terms in Figure 6. It is also possible for the positive and negative eigenvectors to be inverted, for example p_4 in Figure 7

λ	μ	distance	cosine	angle
0.0001	1.0	5.9 ± 0.2	0.73 ± 0.02	$43^\circ \pm 1^\circ$
0.0001	64.5	5.9 ± 0.1	0.73 ± 0.01	$43^\circ \pm 1^\circ$
0.001	1.0	7.4 ± 0.1	0.57 ± 0.01	$55^\circ \pm 1^\circ$
0.001	64.5	8.2 ± 0.1	0.47 ± 0.01	$62^\circ \pm 1^\circ$

Table 2: RMS distance, mean cosine similarity and mean angle between independently trained principal component encodings for CelebA.

(a) and (c), which would show up in Figure 6 as diagonal terms which are negative (red) rather than positive (blue).

In order to resolve these ambiguities and try to bring the two embeddings into approximate alignment, we devised a simple algorithm (shown in the Appendix) which iteratively permutes the principal components in order to increase the (training set) covariance along the diagonal, and adjusts the signs so that all the diagonal terms are positive. The alignment algorithm is not part of the autoencoder itself, but is simply a diagnostic tool to test the similarity of the encodings from different runs. We do not claim that it is optimal; however, it does seem to give good results in practice. Its effect can be visualized by comparing the (test set) correlations on the left of Figure 6 with those on the right. The alignment has the effect of bringing the correlation closer to the diagonal, and turning it from negative (red) to positive (blue). The correlation matrix appears to be more heavily concentrated along the diagonal for $\lambda = 0.0001$ than for 0.001. The appearance of a 2-by-2 block along the diagonal with three blue squares and one red square, such as in the top left corner of Figure 6(c), is indicative of a rotation in the 2-dimensional subspace formed by these two components.

Table 2 shows the RMS distance, mean cosine similarity and mean angle between encodings of the same (test set) images, averaged across six pairwise combinations of four runs, for different choices of λ and μ . We see that the encodings are closer for $\lambda = 0.0001$ than for $\lambda = 0.001$ and that, for $\lambda = 0.001$, they are closer for $\mu = 1$ than for $\mu = 64.5$.

The relative stability of these deep principal components across different runs gives us hope that they may serve as the basis for a data analysis tool, or even an interactive interface for generating desired images. Suppose, for example, that we wish to further explore the effect of components $p_2, p_3, p_6, p_9, p_{10}$ and p_{11} . We could generate a plot such as that shown in Figure 9 by making the selected coordinates positive and negative in all possible combinations.

4.3 Downstream Classification

Another way to test the efficacy of an autoencoder is to train a classifier on the latent variables using different subsets of labeled training items and measure the performance. Table 3 shows the result of training a KNN classifier on subsets of labeled training items of the specified size, averaged across three autoencoder runs and 20 random subsets for each run. The results for $d = 8$ and training size ≥ 100 turn out to be very close (in fact, within the margin of error) to those reported for IRMAE in (Jing et al., 2020) although in that case an MLP with two fully connected layers of dimension 128 was used for classification rather than KNN.

Table 4 shows the classification error averaged across 40 standard binary features for CelebA, using a Decision Tree with depth 1 (also known as a Stump), a Decision Tree with depth 8, and a KNN with 20 neighbors. As a baseline, choosing the majority class in each case would achieve an error rate of 20.0%.

	10(1)	100(1)	1000(5)	10000(10)	60000(15)
$d=2$	39.0 \pm 7.2	19.1 \pm 2.6	12.4 \pm 1.3	10.9 \pm 0.9	10.6 \pm 0.8
$d=4$	36.0 \pm 6.6	12.1 \pm 1.9	5.4 \pm 0.6	4.0 \pm 0.3	3.7 \pm 0.3
$d=6$	33.7 \pm 7.3	10.0 \pm 1.3	4.1 \pm 0.3	3.0 \pm 0.1	2.6 \pm 0.1
$d=8$	34.0 \pm 5.1	9.5 \pm 1.1	3.7 \pm 0.2	2.4 \pm 0.1	2.0 \pm 0.1

Table 3: Error Rate for Downstream Classification on MNIST with different numbers of labeled training items, using a KNN classifier (with the number of neighbors specified in parentheses).

λ	μ	DT(1)	DT(8)	KNN(20)
0.0001	1.0	16.68 \pm 0.12	14.42 \pm 0.11	13.15 \pm 0.03
0.0001	64.5	17.65 \pm 0.33	14.56 \pm 0.16	13.14 \pm 0.04
0.001	1.0	17.61 \pm 0.37	15.20 \pm 0.19	13.30 \pm 0.01
0.001	64.5	17.90 \pm 0.32	15.52 \pm 0.17	13.43 \pm 0.02

Table 4: Classification error averaged over 40 attributes for CelebA dataset, using Decision Tree of depth 1 (Stump), Decision Tree with maximum depth 8, and KNN with 20 neighbors.

Attribute	Component	Information Gain
3. Attractive	$p2$	50% \rightarrow 65%
19. Heavy Makeup	$p2$	60% \rightarrow 76%
20. High Cheek Bones	$p2$	52% \rightarrow 68%
21. Male	$p2$	61% \rightarrow 80%
22. Mouth Slightly Open	$p6$	50% \rightarrow 66%
32. Smiling	$p6$	50% \rightarrow 67%
37. Wearing Lipstick	$p2$	52% \rightarrow 79%

Table 5: Attributes for which a single principal component provides a significant information gain.

Attributes for which a single component provides a significant information gain are listed in Table 5, with reference to the principal components shown in Figure 8. According to Table 5, the images in the upper half of Figure 9 should appear more attractive, more female, with higher cheek bones, wearing lipstick and heavier makeup, compared to those in the lower half. Those in the right half should be smiling with mouth slightly open, compared to those on the left.

5 Conclusion

We have introduced the Eccentric Loss function and shown that it reaches its minimum on a hyperspherical distribution in dimension d with radius very close to \sqrt{d} .

By adjusting the scaling factor, we can force the items to adhere closely to the hypersphere, or we can enable more flexibility and tolerance of eccentricity, thus allowing the latent factors to be stratified according to their relative importance. Because the resulting spectrum and deep principal components are very similar

from one training run to another, our method has the potential to be used as a tool for data visualization and analysis.

In ongoing work, we are exploring potential applications of eccentric regularization to recurrent networks and reinforcement learning. It would also be interesting to see if our approach could be used as a pre-processing step which is then combined with other analytical tools, or with compressive methods like IRMAE.

References

- Bao, Y., Jiang, H., Dai, L., and Liu, C. (2013). Incoherent training of deep neural networks to de-correlate bottleneck features for speech recognition. In *ICASSP*, pages 6980–6984.
- Davidson, T. R., Falorsi, L., Cao, N. D., Kipf, T., and Tomczak, J. M. (2018). Hyperspherical variational auto-encoders. In Globerson, A. and Silva, R., editors, *UAI*, pages 856–865.
- Ghosh, P., Sajjadi, M. S. M., Vergari, A., Black, M. J., and Schölkopf, B. (2020). From variational to deterministic autoencoders. In *ICLR*.
- Grover, A. and Ermon, S. (2019). Uncertainty autoencoders: Learning compressed representations via variational information maximization. In *AISTATS*, pages 2514–2524.
- Heusel, M., Ramsauer, H., Unterthiner, T., Nessler, B., and Hochreiter, S. (2017). GANs trained by a two time-scale update rule converge to a local nash equilibrium. In *NeurIPS*, pages 6626–6637.
- Higgins, I., Matthey, L., Pal, A., Burgess, C., Glorot, X., Botvinick, M., Mohamed, S., and Lerchner, A. (2017). beta-vae: Learning basic visual concepts with a constrained variational framework. In *ICLR*.
- Jing, L., Zbontar, J., et al. (2020). Implicit rank-minimizing autoencoder. *NeurIPS*.
- Kingma, D. P. and Welling, M. (2014). Auto-encoding variational bayes. In *ICLR*.
- LeCun, Y., Bottou, L., Bengio, Y., and Haffner, P. (1998). Gradient-based learning applied to document recognition. *Proceedings of the IEEE*, 86(11):2278–2324.
- Lin, R., Liu, W., Liu, Z., Feng, C., Yu, Z., Rehg, J. M., Xiong, L., and Song, L. (2020). Regularizing neural networks via minimizing hyperspherical energy. In *CVPR*, pages 6917–6927.
- Liu, W., Lin, R., Liu, Z., Liu, L., Yu, Z., Dai, B., and Song, L. (2018). Learning towards minimum hyperspherical energy. In *NeurIPS*, pages 6222–6233.
- Liu, Z., Luo, P., Wang, X., and Tang, X. (2015). Deep learning face attributes in the wild. In *ICCV*, pages 3730–3738.
- Thomson, J. J. (1904). On the structure of the atom: an investigation of the stability and periods of oscillation of a number of corpuscles arranged at equal intervals around the circumference of a circle; with application of the results to the theory of atomic structure. *The London, Edinburgh, and Dublin Philosophical Magazine and Journal of Science*, 7(39):237–265.
- Tolstikhin, I., Bousquet, O., Gelly, S., and Schölkopf, B. (2018). Wasserstein auto-encoders. In *ICLR*.

- van den Oord, A., Vinyals, O., and Kavukcuoglu, K. (2017). Neural discrete representation learning. In *NeurIPS*, pages 6306–6315.
- Xie, P., Deng, Y., and Xing, E. (2015). Diversifying restricted boltzmann machine for document modeling. In *Proceedings of the 21th ACM SIGKDD International Conference on Knowledge Discovery and Data Mining*, pages 1315–1324.
- Xie, P., Singh, A., and Xing, E. P. (2017). Uncorrelation and evenness: a new diversity-promoting regularizer. In *ICML*, pages 3811–3820.
- Yu, Y., Li, Y.-F., and Zhou, Z.-H. (2011). Diversity regularized machine. In *IJCAI*.

A Appendix

A.1 Proof of Theorem 1

The Spherical Distribution \mathcal{S}_ρ will be a stationary point provided the integral, over \mathcal{S}_ρ , of the gradient of $K(\mathbf{z}_0, \mathbf{z}_\rho)$ is equal to zero for any arbitrary point \mathbf{z}_0 on the sphere, i.e.

$$\int_{\mathbf{z}_\rho \in \mathcal{S}_\rho} \nabla_{\mathbf{z}_0} K(\mathbf{z}_0, \mathbf{z}_\rho) d\mathbf{z}_\rho = 0.$$

Equivalently,

$$\int_{\mathcal{S}_\rho} \frac{2\mu(\mathbf{z}_0 - \mathbf{z}_\rho)}{1 + \frac{\|\mathbf{z}_0 - \mathbf{z}_\rho\|^2}{N}} d\mathbf{z}_\rho = \mathbf{z}_0.$$

By symmetry, the integral on the left hand side is a vector in the same direction as \mathbf{z}_0 . We compute its magnitude using the angle $\theta = \cos^{-1}(-z/\rho)$, where z is the component of \mathbf{z}_ρ in the direction of \mathbf{z}_0 . The locus of points $\mathbf{z}_\rho \in \mathcal{S}_\rho$ for which this angle is between θ and $\theta + d\theta$ is an interval of length $\rho d\theta$ crossed with a sphere of dimension $(d-2)$ with radius $\rho \sin \theta$ and surface area $(2\pi^{\frac{d-1}{2}}/\Gamma(\frac{d-1}{2}))(\rho \sin \theta)^{d-2}$. For each point \mathbf{z}_ρ , the component of $(\mathbf{z}_0 - \mathbf{z}_\rho)$ in the direction of \mathbf{z}_0 is $\mathbf{z}_0(1 + \cos \theta)$. Furthermore,

$$\|\mathbf{z}_0 - \mathbf{z}_\rho\|^2 = 4\rho^2 \sin^2\left(\frac{\pi - \theta}{2}\right) = 2\rho^2(1 + \cos \theta).$$

Rewriting $(\sin \theta)^{d-2}$ as $(1 - \cos^2 \theta)^{\frac{d-3}{2}}(\sin \theta)$ and dividing by the surface area $\rho^{d-1}2\pi^{\frac{d}{2}}/\Gamma(\frac{d}{2})$ for normalization, we have

$$\begin{aligned} \int_{\mathcal{S}_\rho} \frac{2\mu(\mathbf{z}_0 - \mathbf{z}_\rho)}{1 + \frac{\|\mathbf{z}_0 - \mathbf{z}_\rho\|^2}{N}} d\mathbf{z}_\rho &= \mathbf{z}_0 \frac{\Gamma(\frac{d}{2})}{\Gamma(\frac{d-1}{2})} \int_{\theta=0}^{\pi} \frac{2\mu(1 + \cos \theta)}{\sqrt{\pi}} \frac{(1 - \cos^2 \theta)^{\frac{d-3}{2}}}{1 + \frac{2\rho^2(1 + \cos(\theta))}{N}} \sin \theta d\theta \\ &= \mathbf{z}_0 \frac{2\mu}{\sqrt{\pi}} \frac{\Gamma(\frac{d}{2})}{\Gamma(\frac{d-1}{2})} \int_{\theta=0}^{\pi} \frac{(1 + \cos \theta)^{\frac{d-1}{2}} (1 - \cos \theta)^{\frac{d-3}{2}}}{1 + \frac{2\rho^2(1 + \cos(\theta))}{N}} \sin \theta d\theta. \end{aligned}$$

We change variables to $u = 1 + \frac{1 + \cos \theta}{a}$, where $a = N/(2\rho^2)$, $\rho = \sqrt{N/2a}$. Then

$$\cos \theta = a(u - 1) - 1, \quad du = -\frac{1}{a} \sin \theta d\theta.$$

So

$$\int_{\mathcal{S}_\rho} \frac{2\mu(\mathbf{z}_0 - \mathbf{z}_\rho)}{1 + \frac{\|\mathbf{z}_0 - \mathbf{z}_\rho\|^2}{N}} d\mathbf{z}_\rho = \mathbf{z}_0 \frac{2a\mu}{\sqrt{\pi}} \frac{\Gamma(\frac{d}{2})}{\Gamma(\frac{d-1}{2})} \int_{u=1}^{1+\frac{2}{a}} \frac{(a(u-1))^{\frac{d-1}{2}} (2 - a(u-1))^{\frac{d-3}{2}}}{u} du.$$

Hence, the spherical distribution \mathcal{S}_ρ is stationary, provided the expression on the right hand side is equal to \mathbf{z}_0 .

A.2 Finding an Approximate Value for N

If d and μ are given, we would like to choose N in such a way that the radius ρ of the stable spherical distribution for $l_{\mu,N}$ is very close to \sqrt{d} . Let us define

$$f_{d,a}(u) = \frac{2a}{\sqrt{\pi}} \frac{\Gamma(\frac{d}{2})}{\Gamma(\frac{d-1}{2})} \frac{(a(u-1))^{\frac{d-1}{2}} (2 - a(u-1))^{\frac{d-3}{2}}}{u},$$

and let a_0 be the value of a for which $\int_{u=1}^{1+\frac{2}{a}} f_{d,a}(u) du = \frac{1}{\mu}$. It follows from Theorem 1 that $\rho = \sqrt{N/2a_0} = \sqrt{d}$ when $N = 2da_0$. We can use the following Lemma to find a good approximation a_1 for a_0 and hence a good choice $N = 2da_1$ for N .

Lemma.

(a) For $d \geq 3$ and $0 < a < 2$,

$$\int_{u=1}^{1+\frac{2}{a}} u f_{d,a}(u) du = 2.$$

(b) For $d \geq 4$, the value $u_{(d,a)}$ of u for which $f_{d,a}(u)$ is maximal satisfies the equation

$$a = \left(1 + \frac{1}{u_{(d,a)}(d-3) + 1}\right) / (u_{(d,a)} - 1).$$

Proof: (See below)

If we assume that $f_{d,a}$ is approximately Gaussian, then the mean value of u when averaged with weighting $f(u)$ should be approximately equal to the value $u_{(d,a)}$ at which $f(u)$ is maximal, i.e.

$$\left(\int_{u=1}^{1+\frac{2}{a}} u f(u) du\right) / \left(\int_{u=1}^{1+\frac{2}{a}} f(u) du\right) \simeq u_{(d,a)}.$$

If a were chosen such that $u_{(d,a)} = 2\mu$, we would have

$$\int_{u=1}^{1+\frac{2}{a}} f(u) du \simeq \left(\int_{u=1}^{1+\frac{2}{a}} u f(u) du\right) / u_{(d,a)} = \frac{2}{2\mu} = \frac{1}{\mu}.$$

From Part (b) of the Lemma, this corresponds to

$$a \simeq \left(1 + \frac{1}{2\mu(d-3) + 1}\right) / (2\mu - 1).$$

In practice, the distribution is slightly skewed, and the true mean is a bit larger than $u_{(d,a)}$. In order to correct for this difference, we replace $(2\mu(d-3) + 1)$ with $2\mu(d-1)$ in the above formula, giving us

$$N = 2da \simeq 2da_1 = 2d\left(1 + \frac{1}{2\mu(d-1)}\right) / (2\mu - 1).$$

Proof of Lemma:

(a) We prove equivalently that $F_{d,a} = G_{d,a}$ where

$$F_{d,a} = \int_{u=1}^{1+\frac{2}{a}} (a(u-1))^{\frac{d-1}{2}} (2-a(u-1))^{\frac{d-3}{2}} du,$$

$$G_{d,a} = \frac{\sqrt{\pi}}{a} \frac{\Gamma(\frac{d-1}{2})}{\Gamma(\frac{d}{2})}.$$

Change variables to

$$a(u-1) = \frac{2}{t^2 + 1}, \quad du = \frac{-4t}{a(t^2 + 1)^2} dt.$$

Then

$$F_{d,a} = \frac{1}{a} \int_0^\infty \left(\frac{2}{t^2+1} \right)^{\frac{d-1}{2}} \left(\frac{2t^2}{t^2+1} \right)^{\frac{d-3}{2}} \frac{4t}{(t^2+1)^2} dt = \frac{2^d}{a} \int_0^\infty \frac{t^{d-2}}{(t^2+1)^d} dt.$$

If we set

$$J(k, n) = \int_0^\infty \frac{t^k}{(t^2+1)^n} dt,$$

then $J(0, 1) = \frac{\pi}{2}$, $J(1, n) = \frac{1}{2(n-1)}$ for $n \geq 2$, and we can derive these recurrences for $n, k \geq 2$:

$$J(k, n) = \frac{k-1}{2(n-1)} J(k-2, n-1), \quad J(0, n) = \frac{2n-3}{2n-2} J(0, n-1).$$

It follows that when $d \geq 2$ is even,

$$\begin{aligned} F_{d,a} &= \frac{2^d}{a} J(d-2, d) = \frac{2^d}{a} \frac{(d-3)!! \left(\frac{d}{2}\right)!}{2^{\frac{d-2}{2}} (d-1)!} J(0, \frac{d+2}{2}) \\ &= \frac{2^d}{a} \frac{(d-3)!! \left(\frac{d}{2}\right)!}{2^{\frac{d-2}{2}} (d-1)!} \frac{(d-1)!! \pi}{d!! \cdot 2} \\ &= \frac{\pi}{a} \frac{(d-3)!! \cdot 2^{\frac{d}{2}} \left(\frac{d}{2}\right)! (d-1)!!}{(d-2)!! \cdot d \cdot (d-1)!} \\ &= \frac{\pi (d-3)!!}{a (d-2)!!} = G_{d,a}. \end{aligned}$$

When $d \geq 3$ is odd,

$$\begin{aligned} F_{d,a} &= \frac{2^d}{a} J(d-2, d) = \frac{2^d}{a} \frac{(d-3)!! \left(\frac{d+1}{2}\right)!}{2^{\frac{d-3}{2}} (d-1)!} J(1, \frac{d+3}{2}) \\ &= \frac{2}{a} \frac{(d-3)!! \cdot 2^{\frac{d+1}{2}} \left(\frac{d+1}{2}\right)!}{(d-1)! \cdot 2 \left(\frac{d+1}{2}\right)!} \\ &= \frac{2}{a} \frac{(d-3)!! (d+1)!!}{(d-1)! (d+1)} \\ &= \frac{2 (d-3)!!}{a (d-2)!!} = G_{d,a}. \end{aligned}$$

(b) When $d \geq 4$, the derivative of $f_{d,a}(u)$ is $C_{(d,a)} D_{(d,a)}$ where

$$\begin{aligned} C_{(d,a)} &= \frac{-2a^2}{\sqrt{\pi}} \frac{\Gamma(\frac{d}{2})}{\Gamma(\frac{d-1}{2})} (a(u-1))^{\frac{d-3}{2}} (2-a(u-1))^{\frac{d-5}{2}}, \\ D_{(d,a)} &= (a(u-1)-1)(u(d-3)+1)-1. \end{aligned}$$

This derivative will be zero when $D_{(d,a)} = 0$, i.e. when

$$a = \left(1 + \frac{1}{u(d-3)+1}\right) / (u-1).$$

A.3 Alignment Algorithm

Algorithm 1 Alignment Algorithm

Input: $E_1 : I \mapsto (p_1, \dots, p_d)$ and $E_2 : I \mapsto (q_1, \dots, q_d)$

Output: E_1, E_2 with coordinates permuted and/or negated

```

1: repeat
2:   sorted = true
3:   for  $i = 1$  to  $d$  do
4:      $j = \operatorname{argmax}_{j_0 \in [i, d]} |\langle p_{j_0}, q_i \rangle|$ 
5:      $k = \operatorname{argmax}_{k_0 \in [i, d]} |\langle p_i, q_{k_0} \rangle|$ 
6:     if  $j > i$  and  $|\langle p_j, q_i \rangle| > |\langle p_i, q_k \rangle|$  then
7:       sorted = false
8:       permute  $(p_i \rightarrow p_{i+1} \rightarrow \dots \rightarrow p_{j-1} \rightarrow p_j \rightarrow p_i)$ 
9:       if  $\langle p_i, q_i \rangle < 0$  then
10:         $p_i = -p_i$ 
11:     else if  $k > i$  then
12:       sorted = false
13:       permute  $(q_i \rightarrow q_{i+1} \rightarrow \dots \rightarrow q_{k-1} \rightarrow q_k \rightarrow q_i)$ 
14:       if  $\langle p_i, q_i \rangle < 0$  then
15:         $q_i = -q_i$ 
16:   until sorted == true
17:   for  $i = 1$  to  $d$  do
18:      $k = \operatorname{argmax}_{k_0 \in [i, d]} (\langle p_{k_0}, p_{k_0} \rangle + \langle q_{k_0}, q_{k_0} \rangle)$ 
19:     if  $k > i$  then
20:       permute  $(q_i \rightarrow q_{i+1} \rightarrow \dots \rightarrow q_{k-1} \rightarrow q_k \rightarrow q_i)$ 
21:       permute  $(p_i \rightarrow p_{i+1} \rightarrow \dots \rightarrow p_{k-1} \rightarrow p_k \rightarrow p_i)$ 
22: return solution

```

A.4 Pytorch code for Eccentric Loss function

```

def EccentricLoss( z, scale=1 ):
    x0 = torch.squeeze(z)
    x1 = x0.transpose(0,1)
    batch = x0.size()[0]
    dim = x0.size()[1]
    norm = 2*dim*(1 + 1/(2*scale*(dim-1)))/(2*scale-1)
    xx = torch.bmm(x0.view(batch,1,dim),
                   x0.view(batch,dim,1)).squeeze(2)
    xx0 = xx.expand(batch,batch)
    xx1 = xx0.transpose(0,1)
    xy = xx0 + xx1 - 2*torch.matmul(x0,x1)
    result = torch.sum(xx) - scale*norm*torch.sum(
        torch.log(1+xy/norm))/(batch-1)
    return result/batch

```

A.5 Network Architectures

Encoder architecture for MNIST:

$$\begin{aligned}
x \in \mathcal{R}^{32 \times 32 \times 1} &\rightarrow \text{Conv}_{16}^{5(1)} \rightarrow \text{BN} \rightarrow \text{LeakyReLU}_{(0.1)} \\
&\rightarrow \text{Conv}_{24}^{4(2)} \rightarrow \text{BN} \rightarrow \text{LeakyReLU}_{(0.1)} \\
&\rightarrow \text{Conv}_{32}^{4(1)} \rightarrow \text{BN} \rightarrow \text{LeakyReLU}_{(0.1)} \\
&\rightarrow \text{Conv}_{48}^{4(2)} \rightarrow \text{BN} \rightarrow \text{LeakyReLU}_{(0.1)} \\
&\rightarrow \text{FC}_{64} \rightarrow \text{FC}_d
\end{aligned}$$

Decoder architecture for MNIST:

$$\begin{aligned}
x \in \mathcal{R}^d &\rightarrow \text{FSConv}_{48}^{3(1)} \rightarrow \text{BN} \rightarrow \text{LeakyReLU}_{(0.1)} \\
&\rightarrow \text{FSConv}_{32}^{4(2)} \rightarrow \text{BN} \rightarrow \text{LeakyReLU}_{(0.1)} \\
&\rightarrow \text{FSConv}_{24}^{4(1)} \rightarrow \text{BN} \rightarrow \text{LeakyReLU}_{(0.1)} \\
&\rightarrow \text{FSConv}_{16}^{4(2)} \rightarrow \text{BN} \rightarrow \text{LeakyReLU}_{(0.1)} \\
&\rightarrow \text{FSConv}_{16}^{5(1)} \rightarrow \text{BN} \rightarrow \text{LeakyReLU}_{(0.1)} \\
&\rightarrow \text{FSConv}_{16}^{1(1)} \rightarrow \text{BN} \rightarrow \text{LeakyReLU}_{(0.1)} \\
&\rightarrow \text{FSConv}_1^1 \rightarrow \text{Sigmoid}
\end{aligned}$$

Encoder architecture for CelebA:

$$\begin{aligned}
x \in \mathcal{R}^{64 \times 64 \times 3} &\rightarrow \text{Conv}_{128}^{4(2)} \rightarrow \text{BN} \rightarrow \text{ReLU} \\
&\rightarrow \text{Conv}_{256}^{4(2)} \rightarrow \text{BN} \rightarrow \text{ReLU} \\
&\rightarrow \text{Conv}_{512}^{4(2)} \rightarrow \text{BN} \rightarrow \text{ReLU} \\
&\rightarrow \text{Conv}_{1024}^{4(2)} \rightarrow \text{BN} \rightarrow \text{ReLU} \rightarrow \text{FC}_{64}
\end{aligned}$$

Decoder architecture for CelebA:

$$\begin{aligned}
x \in \mathcal{R}^{64} &\rightarrow \text{FC}_{8 \times 8 \times 1024} \\
&\rightarrow \text{FSConv}_{512}^{4(2)} \rightarrow \text{BN} \rightarrow \text{ReLU} \\
&\rightarrow \text{FSConv}_{256}^{4(2)} \rightarrow \text{BN} \rightarrow \text{ReLU} \\
&\rightarrow \text{FSConv}_{128}^{4(2)} \rightarrow \text{BN} \rightarrow \text{ReLU} \\
&\rightarrow \text{FSConv}_3^1 \rightarrow \text{Sigmoid}
\end{aligned}$$

Metaparameters for all networks:

optimizer: Adam
batch size: 100
learning rate: 0.0001
weight decay: 0.000001